Randomization of the Earth's magnetic field driven by magnetic helicty

Alexander Bershadskii

ICAR, P.O. Box 31155, Jerusalem, 91000, Israel
(bershads@gmail.com)

Abstract

It is shown, using results of numerical simulations and geomagnetic observations, that the spatial and temporal randomization of the Earth's global and local magnetic fields is driven by magnetic helicity (ideal magnetohydrodynamic invariant). In the frames of the distributed chaos notion, the magnetic helicity determines the degree of magnetic field randomization and the results of numerical simulations are in quantitative agreement with the geophysical observations despite the considerable differences in the scales and physical parameters.

1. Introduction

Usually, the magnetic helicity is related to the process of generation of a mean magnetic field (dynamo). In this paper, we do not investigate this mechanism in detail. Instead, the process of *randomization* of the magnetic field driven by the magnetic helicity is the main subject of the present investigation.

The concept of smoothness can be functional for the quantitative classification of the non-laminar regimes in magnetohydrodynamics (and in fluid dynamics in general) according to their randomness. The spectral analyses can be used for this purpose. Namely, the stretched exponential spectra are typical for the smooth magnetohydrodynamics

$$E(k) \propto \exp{-(k/k_\beta)^\beta} \qquad (1)$$

here $1 \geq \beta > 0$ and k is the wavenumer. The value $\beta = 1$

$$E(k) \propto \exp(-k/k_c) \qquad (2)$$

is typical for deterministic chaos (see Frisch and Morf, 1981; Brandstater and Swinney, 1987; Maggs and Morales, 2011, 2012; Khurshid et al,, 2018).

For $1 > \beta$ the dynamics is still smooth but not deterministic (and will be called the distributed chaos, see below for clarification of the term). It can be also considered as a soft turbulence (Wu et al., 1990).

The non-smooth (hard turbulence Wu et al., 1990) dynamics is typically characterized by the power-law (scaling) spectra.

In this approach, the value of the β can be considered as a proper measure
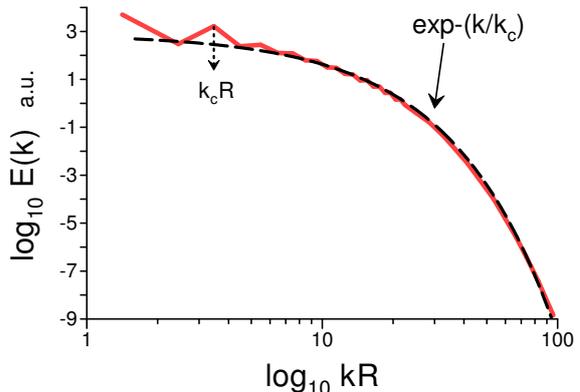
Figure 1: Magnetic energy spectrum $E(k)$ generated by a chaotic magnetohydrodynamic dynamo in a conducting spherical Couette flow at $Pr_m = 0.25$ (a direct numerical simulation).

of randomization. Namely, the further the value of the parameter β is from the deterministic $\beta = 1$ (i.e. smaller the β) the randomization is stronger.

More intensive chaotic/randomized flows naturally support more randomized magnetic fields. The degree of randomization of the magnetic field depends also on the magnetic parameters (such as the magnetic Prandtl number Pr_m and magnetic Reynolds number Re_m.

The ideal magnetohydrodynamics has three quadratic (fundamental) invariants: total energy, cross, and magnetic helicity (see, for instance, paper Moffatt and Tsinober, 1992).

The magnetic helicity is

$$h_m = \langle \mathbf{A} \cdot \mathbf{B} \rangle \qquad (3)$$

where the magnetic field is $\mathbf{B} = [\nabla \times \mathbf{A}]$ ($\nabla \cdot \mathbf{A} = 0$), and a spatial average is denoted as $\langle ... \rangle$.

2

In the next sections, the observed in the numerical simulations and geophysical observations values of β will be related to the magnetic helicity. These relationships allow a deeper understanding of the physics of randomization of the magnetic field in the chaotic flows.

Figure 1 shows (as an example) the magnetic energy spectrum $E(k)$ (against the wavenumber k) generated by a magnetohydrodynamic dynamo in a conducting spherical Couette flow at the magnetic Prandtl number $Pr_m = \nu/\eta = 0.25$ (here ν is the kinematic viscosity and η is the magnetic diffusivity of the fluid) and the Ekman number $E = \nu/(\Omega r_o^2) = 10^{-3}$ (here Ω is the rotational rate of the outer sphere and r_o is its radius). This is a flow between two concentric spheres with a differential rotation relevant to the Earth's outer liquid core. To simulate the situation in the Earth's core the aspect ratio $r_i/r_o = 0.35$ (here r_i is the radius of the inner core, see for more details Guervilly and Cardin, 2010).

The spectral data were taken from Fig. 13 of the Ref. (Guervilly and Cardin, 2010). The spectra were time and r averaged over the whole shell. R is an effective radius ($r_i < R < r_o$) and the wave number $k = \sqrt{l(l+1)}/R$ where l is the spherical harmonic degree (cf Section 4.1).

The dashed curve indicates the best fit with the exponential Eq. (2) (the deterministic chaos), and the dotted vertical arrow indicates the position of the k_c. As one can see the small-scale dynamo coexists with the large-scale dynamo and the large-scale coherent structures determine the deterministic chaos in this case (the position of the $k_c R$ coincides with the position of the spectral peak indicating the coherent structures).

2. Distributed chaos in magnetic field driven by magnetic helicity

The randomization can be also described using a probabilistic approach, i.e. introducing a probability distribution $P(k_c)$ characterizing the random fluctuations of the characteristic scale k_c

$$E(k) \propto \int_0^\infty P(k_c) \exp -(k/k_c) dk_c \qquad (4)$$

Therefore, the corresponding smooth non-deterministic chaotic dynamics can be named 'distributed chaos'.

One can find the probability distribution $P(k_c)$ for the magnetohydrodynamics dominated by the magnetic helicity using the dimensional considerations and a scaling relationship

$$B_c \propto |h_m|^{1/2} k_c^{1/2} \qquad (5)$$

relating the characteristic value of the magnetic field B_c to the characteristic value of the wavenumber k_c.

If the positive variable B_c has the half-normal probability distribution $P(B_c) \propto \exp -(B_c^2/2\sigma^2)$ (Monin and Yaglom, 2007) (it is a normal distribution with zero mean truncated to only have nonzero probability density for positive values of its argument: if B is a normal random variable, then $B_c = |B|$ has a half-normal distribution Johnson et al. 1994), then it follows from Eq. (5) that the characteristic value of the wavenumber k_c has the chi-squared (χ^2) distribution

$$P(k_c) \propto k_c^{-1/2} \exp -(k_c/4k_\beta) \qquad (6)$$

here k_β is a new constant.

Substituting Eq. (6) into Eq. (4) we obtain

$$E(k) \propto \exp -(k/k_\beta)^{1/2} \qquad (7)$$

3. Magneto-inertial range of scales

In hydrodynamic turbulence presence of an inertial range of scales is expected for the high Reynolds numbers. In this range, the statistical characteristics of the motion depend on the kinetic energy dissipation rate ε only (Monin and Yaglom, 2007). In magnetohydrodynamics, a magneto-inertial range of scales can be introduced. In this range two parameters: the magnetic helicity dissipation rate ε_h and the total energy dissipation rate ε govern the magnetic field dynamics. An analogous situation with two governing parameters (kinetic dissipation rate and the passive scalar dissipation rate) was studied for the inertial-convective range in the Corrsin-Obukhov approach (Monin and Yaglom, 2007; see also Bershadskii and Sreenivasan, 2004). Let us, following this analogy, replace the estimate Eq. (5) by the estimate

$$B_c \propto \varepsilon_h^{1/2}\ \varepsilon^{-1/6}\ k_c^{1/6} \qquad (8)$$

for the magneto-inertial range dominated by magnetic helicity.

The estimates Eq. (5) and (8) can be generalized as

$$B_c \propto k_c^{\alpha} \qquad (9)$$

Let us look for the spectrum of the distributed chaos as a stretched exponential (see Introduction and Eq. (7))

$$E(k) \propto \int_0^{\infty} P(k_c) \exp{-(k/k_c)}dk_c \propto$$

$$\propto \exp{-(k/k_\beta)^{\beta}} \qquad (10)$$

The Eq. (10) can be used to estimate the probability distribution $P(k_c)$ for large k_c (Johnston, 2006)

$$P(k_c) \propto k_c^{-1+\beta/[2(1-\beta)]}\ \exp(-\gamma k_c^{\beta/(1-\beta)}) \qquad (11)$$

A relationship between the exponents β and α can be readily obtained (using some algebra) from the Eqs. (9) and (11) for the half-normally distributed B_c

$$\beta = \frac{2\alpha}{1+2\alpha} \qquad (12)$$

Since for the magneto-inertial range (dominated by the magnetic helicity) $\alpha = 1/6$ (see Eq. (8)) corresponding magnetic energy spectrum can be estimated using Eq. (12) as

$$E(k) \propto \exp{-(k/k_\beta)^{1/4}} \qquad (13)$$

4. Geodynamo

4.1. Numerical simulations

It is now believed that the magnetic field of Earth is generated by a flow of liquid metal in the Earth's outer core (the geodynamo). Numerical simulations can be rather useful in investigation of this mechanism. The problems with the numerical simulations of the geodynamo are numerous. First of all, it is still very difficult to approach the values of the parameters characteristic of the real geodynamo (see, for instance, Table 1 in a recent paper Schaeffer et al., 2017), it is also difficult to simulate the real boundary and physical conditions for the Earth's core.

In the Ref. (Schaeffer et al., 2017) a recent attempt to this end was made using maximal possibilities of the present computers. The authors of the DNS numerically solved the equations of the thermally (buoyancy) driven convection of an electrically conducting fluid with a chemical species concentration gradient (in the Boussinesq approximation with the Lorentz force) in a

4

rotating spherical shell mimicking the liquid geodynamo confined between the mantle and solid inner core:

$$\partial_t \mathbf{u} + \left(\frac{2}{E} \mathbf{e_z} + \nabla \times \mathbf{u} \right) \times \mathbf{u} = -\nabla p + \Delta \mathbf{u}$$

$$+ (\nabla \times \mathbf{b}) \times \mathbf{b} - \frac{Ra}{\beta} \, C \, \frac{D}{r_o} \mathbf{r} \qquad (14)$$

$$\partial_t \mathbf{b} = \nabla \times (\mathbf{u} \times \mathbf{b}) + \frac{1}{Pr_m} \Delta \mathbf{b} \qquad (15)$$

$$\partial_t C + \mathbf{u} \cdot \nabla (C + C_0) = \frac{1}{Pr} \Delta C \qquad (16)$$

$$\nabla \cdot \mathbf{u} = 0, \quad \nabla \cdot \mathbf{b} = 0 \qquad (17)$$

where the gravity acceleration is proportional to the radius, $C(\mathbf{r})$ is the scalar codensity field (for the chemical species concentration), $C_0(r)$ is the radial conductive codensity profile, β is the codensity gradient, $\mathbf{e_z}$ is the unit vector in the direction of rotation, E is the Ekman number, Ra is the Rayleigh number, D is the shell thickness, r_0 is the outer core boundary radius.

The boundary conditions for $\mathbf{u}$ are no-slip, the mantle and inner solid core are electrically insulating, and deviation of codensity from $C_0(r)$ on the boundaries has zero radial gradient (more details about choosing the $C_0(r)$ and the initial conditions can be found in the Ref. (Schaeffer et al., 2017).

The time-averaged spatial spectral data at the spheres of different radii R were provided in the paper (Schaeffer et al., 2017) for the case with the most vigorous motion: $Re = 5140$, $Ra = 2.54 \times 10^{12}$, $Ro = 5.1 \times 10^{-4}$, $E = 10^{-7}$, $Pr = 1$, $Re_m = 514$, and $Pr_m = 0.1$. The system is helical, and for this case the bulk relative helicity and helicity at the boundaries were
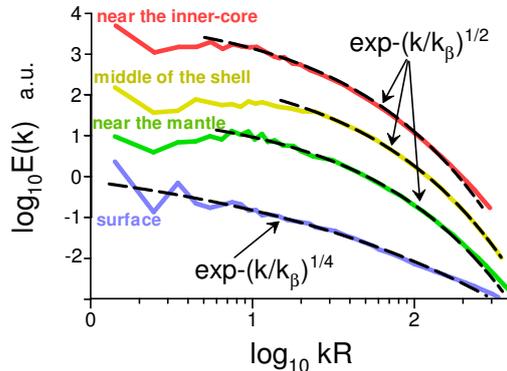
Figure 2: Time-averaged magnetic energy spectra at the spheres of different radii R (numerical simulation). The spectra are vertically shifted for clarity.

also rather strong.

It should be noted that the spectral data were provided in (Schaeffer et al., 2017) as a dependence of the energy density spectra $E(l)$ on the spherical harmonic degree l. On a sphere of radius R the wavenumber k is related to l as

$$kR = \sqrt{l(l+1)} \qquad (18)$$

Figure 2 shows the magnetic energy spectra $E(k)$ against the wavenumber k at the spheres of different radii R (the spectral data were taken from Fig. 13 of the Ref. (Schaeffer et al., 2017) and transformed using the Eq. (18)). The dashed curves indicate the helical spectral law Eq. (7) near the inner-core, in the middle of the shell, and near the mantle, whereas at the surface the spectral law Eq. (13) indicates the magneto-inertial range of scales (a precursor of the hard turbulence see Introduction and (Wu et al., 1990). One can see that in this case the small-scale dynamo coexists with the large-scale one.

Another example of a numerical simulation trying to approach the real conditions

5
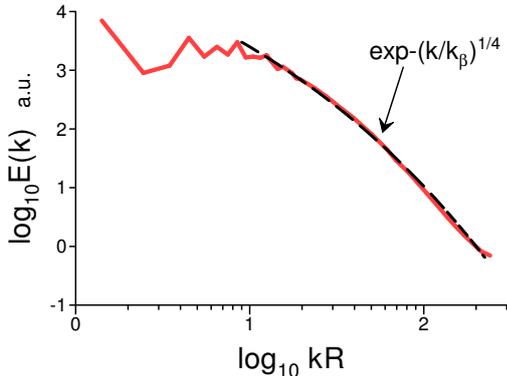
Figure 3: Time-averaged magnetic energy spectrum at the Ekman number $E = 3 \times 10^{-7}$ and $Pr_m = 0.05$ (numerical simulation).

Figure 4: Geomagnetic power spectrum calculated using local subgrids from World Magnetic Anomaly Map of the National Geophysics Data Center (WMAM). The spectra are vertically shifted for clarity.

can be found in a recent paper (Sheyko et al., 2018). In this numerical simulation, the modeled liquid was enclosed in a rotating spherical shell between two radii r_o and r_i and the ratio $r_i/r_o = 0.35$ (as for the Earth, cf the example of numerical simulation in Introduction). Both boundaries of the shell were taken no-slip and impermeable. The outer boundary was electrically insulating, and the inner solid core had the same conductivity as the liquid outer core. The inner core temperature was kept constant. Whereas the gradient of the temperature was kept constant and a uniform heat source was distributed throughout the outer core. The constant heat flux boundary conditions were applied at the core-mantle boundary. The dynamo was initiated and supported by the thermal convection under the strong influence of the rotation (the Ekman number $E = \nu/\Omega(r_o - r_i)^2 = 3 \times 10^{-7}$, the magnetic Prandtl number $Pr_m = \nu/\eta = 0.05$).

Figure 3 shows the magnetic energy spectrum obtained at this numerical simulation (the spectral data were taken from Fig. 3b of the Ref. (Sheyko et al., 2018)). The

spectrum was time and r averaged over the whole shell, R is an effective radius ($r_i < R < r_o$) and the wave number $k = \sqrt{l(l+1)}/R$ where l is the spherical harmonic degree.

The dashed curve indicates the spectral law Eq. (13), i.e. the magneto-inertial range for the small scales. One can see that the small-scale dynamo coexists with the large-scale one in this simulation as well.

4.2. Spatial geomagnetic observations

Figure 4 shows the geomagnetic power spectrum calculated using local subgrids from the World Magnetic Anomaly Map of the National Geophysics Data Center (WMAM, Maus et al., 2007). The data were detrended and azimuthally averaged, and the mean field was subtracted by the author of the Ref. (Maus, 2008). The spectral data for Fig. 4 were taken from Fig. 4 of (Maus, 2008). The land and ocean averages were considered separately (here R is the Earth's radius). The dashed curve indicates the helical spectral law Eq. (7) for the ocean data, whereas at the land the spectral law Eq. (13) indicates the

6
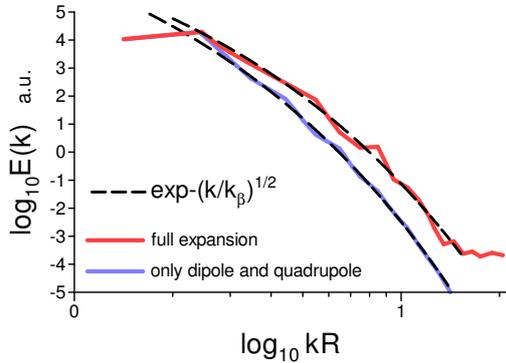
Figure 5: Large-scale globally averaged total geomagnetic intensity spectrum.

Figure 6: Global geomagnetic energy spectrum at the Earth's surface in the period 1999-2020.

magneto-inertial range of scales.

In the paper (Maus, 2008) a large-scale globally averaged total intensity spectrum computed using the spherical harmonic coefficients of the magnetic potential from a C89 global geomagnetic field model C89 (Cain et al., 1089) was also presented. It is interesting to compare the spectral data with the above-suggested spectra. Figure 5 shows the spectral data taken from Fig. 2 of the Ref. (Maus, 2008). The dashed curves indicate the helical spectrum Eq. (7) (here R is the Earth's radius).

Figure 6 shows (in the semi-log scales) the spectral data taken from Fig. 2 of a recent paper (Finlay et al., 2020). The spectral computations were produced using the CHAOS-7 model of the near-Earth magnetic field for the period 1999-2020 based on the observations made by the low-Earth orbit satellites CryoSat-2, Swarm, CHAMP, SAC-C, Orsted, and SAC-C, and on the ground observatory measurements. The dashed curve indicates the helical spectrum Eq. (7) (here R is the Earth's radius).

4.3. Temporal geomagnetic observations

Until now the spatial randomization of the Earth's magnetic field was considered. The above consideration can be readily extended on the frequency spectra $E(f)$ corresponding to the temporal variably. For this purpose, Eq. (8) should be replaced by the equation

$$B_c \propto \varepsilon_h^{1/2} \ \varepsilon^{-1/4} \ f_c^{1/4} \qquad (19)$$

Hence $\alpha = 1/4$ for the case represented by Eq. (19). It follows from the Eq. (12) (which is obviously valid for the frequency spectra as well) that $\beta = 1/3$ for the case of the Eq. (19). Corresponding spectrum has the form

$$E(k) \propto \exp{-(f/f_\beta)^{1/3}} \qquad (20)$$

Figure 7 shows the frequency magnetic energy spectrum obtained using measurements provided by the global magnetic observatory network (the spectral data were taken from Fig. 5 of a recent paper (Constable and Constable, 2023). The range of frequencies shown in the Fig. 7 corresponds to the time scales for which the variability of the magnetic field on Earth is dominated mainly by the variability of
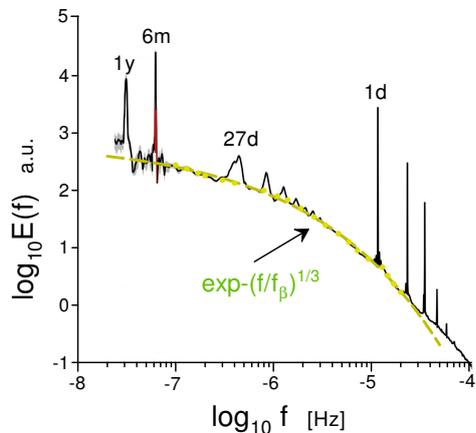
Figure 7: Frequency magnetic energy spectrum obtained using measurements provided by the global magnetic observatory network.

the external magnetic field arising from the interaction of the nearby solar wind with Earth's magnetosphere and its inner edge - ionosphere (see, Fig. 1 of the paper Constable and Constable, 2023 to obtain the entire picture).

The 27-day peak and its harmonics are related to the solar rotation period whereas the peak and its harmonics corresponding to daily variations are presumably associated with thermal electric currents in the ionosphere on the heated day side of the globe. Seasonal variations of the ionosphere heating can be the main reason for the appearance of the spectral peaks corresponding to the 1 year and 6 months (Constable and Constable, 2023).

The dashed curve in the Fig. 7 indicates correspondence to the spectral law Eq. (20) (the magneto-inertial range of scales).

5. Acknowledgments

References

A. Bershadskii, and K.R. Sreenivasan, Intermittency and the passive nature of the magnitude of the magnetic field, Phys. Rev. Lett. 93 (2004) 064501

A. Brandstater and H. L. Swinney, Strange attractors in weakly turbulent Couette-Taylor flow, Phys. Rev. A 35 (1987) 2207-2220

J.C. Cain, Z. Wang, C. Kluth, and D.R. Schmitz, Derivation of a geomagnetic model to n = 63, Geophys. J. Int., 97 (1989) 431-441

C. Constable, and S. Constable, A grand spectrum of the geomagnetic field, Physics of the Earth and Planetary Interiors, 344, (2023) 107090

C.C. Finlay, C. Kloss, N. Olsen, M.D. Hammer et al., The CHAOS-7 geomagnetic field model and observed changes in the South Atlantic Anomaly, Earth, Planets and Space 72 (2020) 156

U. Frisch and R. Morf, Intermittency in nonlinear dynamics and singularities at complex times, Phys. Rev., 23 (1981) 2673-2704

C. Guervilly and P. Cardin, Numerical simulations of dynamos generated in spherical Couette flows, Geophysical & Astrophysical Fluid Dynamics, 104 (2010) 220-248

N.E.L. Haugen, A. Brandenburg, and W. Dobler, Is nonhelical hydromagnetic turbulence peaked at small scales?, ApJ. 597 (2003) L141

R.S. Iroshnikov, Astronomicheskii Zhurnal, Turbulence of a conducting fluid in a strong magnetic field, 40 (1963) 742 (English translation in Soviet Astronomy 7, 566 (1964))

N.L. Johnson, S. Kotz, and N. Balakrishnan, Continuous Univariate Distributions, Vol. 1, (Wiley NY, 1994)

D.C. Johnston, Stretched exponential relaxation arising from a continuous sum of exponential decays, Phys. Rev. B 74 (2006) 184430

S. Khurshid, D.A. Donzis, and K.R. Sreenivasan, Energy spectrum in the dissipation range, Phys. Rev. Fluids 3 (2018) 082601(R)

J.E. Maggs and G.J. Morales, Generality of deterministic chaos, exponential spectra, and Lorentzian pulses in magnetically confined plasmas, Phys. Rev. Lett. 107, (2011) 185003

J.E. Maggs and G.J. Morales, Origin of Lorentzian pulses in deterministic chaos, Phys. Rev. E 86 (2012) 015401(R)

S. Maus, T. Sazonova, K. Hemant, et. al., National Geophysical Data Center candidate for the World Digital Magnetic Anomaly Map,

Geochem. Geophys. Geosystems, 8 (2007) Q06017

S. Maus, Geophys. The geomagnetic power spectrum, J. Int., **174**, 135-142 (2008)

H.K. Moffatt and A. Tsinober, Annu. Rev. Fluid Mech., Helicity in laminar and turbulent flow, 24 (1992) 281-312

A.S. Monin, and A.M. Yaglom, Statistical Fluid Mechanics, Vol. II: Mechanics of Turbulence (Dover Pub. NY, 2007)

N. Schaeffer, D. Jault, H.-C. Nataf, and A. Fournier, Turbulent geodynamo simulations: a leap towards Earth's core, Geophys. J. Int., 211 (2017) 1-29

J.V. Shebalin, Global invariants in ideal magnetohydrodynamic turbulence, Phys. Plasmas 20 (2013) 102305

A. Sheyko, C. Finlay, J. Favre, and A. Jackson, Scale separated low viscosity dynamos and dissipation within the Earth's core, Scientific Reports, 8 (2018) 12566

X.-Z. Wu, L.P. Kadanoff, A. Libchaber and M. Sano, Frequency power spectrum of temperature fluctuations in free convection, Phys. Rev. Lett., 64 (1990) 2140-2143